

Neural Implicit Surface Reconstruction for Freehand 3D Ultrasound Volumetric Point Clouds with Geometric Constraints

Hongbo Chen, Logiraj Kumaralingam, Edmond H. M. Lou, Kumaradevan Punithakumar, Jiawen Li, Thanh-Tu Pham, Lawrence H. Le, Rui Zheng

Abstract

Three-dimensional (3D) freehand ultrasound (US) is a widely used imaging modality that allows non-invasive imaging of medical anatomy without radiation exposure. The freehand 3D US surface reconstruction is vital to acquire the accurate anatomical structures needed for modeling, registration, and visualization. However, the currently used traditional methods cannot produce a high-quality surface due to imaging noise and connectivity issues in US. Although the deep learning-based approaches exhibiting the improvements in smoothness, continuity and resolution, the investigation into freehand 3D US remains limited. In this study, we introduce a self-supervised neural implicit surface reconstruction method to learn the signed distance functions (SDFs) from freehand 3D US volumetric point clouds. In particular, our method iteratively learns the SDFs by moving the 3D queries sampled around the point clouds to approximate the surface with the assistance of two novel geometric constraints. We assess our method on the three imaging systems, using twenty-three shapes that include six distinct anthropomorphic phantoms datasets and seventeen *in vivo* carotid artery datasets. Experimental results on phantoms outperform the existing approach, with a 67% reduction in Chamfer distance, 60% in Hausdorff distance, and 61% in Average absolute distance. Furthermore, our method achieves a 0.92 Dice score on the *in vivo* datasets and demonstrates great clinical potential.

Index Terms

Freehand 3D ultrasound, neural surface reconstruction, 3D point clouds, signed distance function, implicit neural representation

I. INTRODUCTION

A. Motivation

ULTRASOUND (US) is a widely used imaging modality for clinical diagnosis, monitoring and analysis due to its low cost, radiation-free and real-time performance. The 3D US with rich anatomical structure has been greatly developed and applied in many areas, such as structure assessment and standard plane localization [1], [2]. The data acquisition of 3D US imaging can be divided into 2D array, mechanical control, freehand scan without tracking sensor and freehand scan with tracking sensors [3], [4]. Compared to the other three approaches, freehand 3D US with tracking sensors is a rapidly advancing technology to obtain the high-quality 3D volumes without the limitation of field-of-view [5].

The freehand 3D US imaging technology commonly compounds the collected 2D B-mode images from the transducer and the corresponding 3D poses from the tracking device into a volume to reconstruct the 3D internal structures of the human body [6]. After the reconstruction, the volume rendering technique is usually adopted to transmit the 3D information in a translucent way. However, such voxel-based visualization makes it hard to recover accurate geometries and continuous surface. Since each voxel element in the volume is considered for the rendered view, this technique also requires expensive computation cost [7].

The surface reconstruction is an alternate method to facilitate the geometric evaluation, morphological assessment, multi-modality topography, and surgery guidance [8], [9], [10]. Traditional surface reconstruction methods for freehand 3D US, like Contour filtering and Marching Cubes, usually convert the voxel representation after volume reconstruction to triangles or polygons mesh according to the segmented boundary [11]. The geometric connection between each voxel is established

This work was sponsored by Natural Science Foundation of China (NSFC) under Grant No.12074258 and a grant from Alberta Innovates - Accelerating Innovations into CarE (AICE) program under Grant No. RES0056222. (Hongbo Chen and Logiraj Kumaralingam contributed equally.) (Corresponding authors: Lawrence H. Le and Rui Zheng.)

Hongbo Chen is with School of Information Science and Technology, ShanghaiTech University, Shanghai 201210, China, also with Shanghai Advanced Research Institute, Chinese Academy of Sciences, Shanghai 200050, China, and also with University of Chinese Academy of Sciences, Beijing 100049, China.

Logiraj Kumaralingam and Dr. Kumaradevan Punithakumar are with Department of Radiology and Diagnostic Imaging, University of Alberta, Edmonton, T6G 2V2, Canada.

Jiawen Li is with School of Information Science and Technology, ShanghaiTech University, Shanghai 201210, China.

Thanh-Tu Pham, Dr. Edmond H. M. Lou and Dr. Lawrence H. Le are with Department of Biomedical Engineering and Department of Radiology and Diagnostic Imaging, University of Alberta, Edmonton, T6G 2V2, Canada (e-mail: lawrence.le@ualberta.ca).

Dr. Rui Zheng is with School of Information Science and Technology, Shanghai Engineering Research Center of Intelligent Vision and Imaging, ShanghaiTech University, Shanghai, China (e-mail: zhengrui@shanghaitech.edu.cn).

following the successive slices or voxel intensity, also known as the ISO-Surface [12]. However, the traditional methods have connectivity problem because of the empty holes or noise in the reconstructed US volume, this will lead to a rough surface, which requires further post-processing, such as smoothing and interpolation for better reconstruction results. The quality of the generated surface is also limited by the original reconstructed volume and the voxel resolution [13].

In recent years, there has been a growing interest in using deep learning (DL) approaches for surface reconstruction from medical imaging data, as an alternative to traditional methods, to bring increased accuracy and speed, as well as the ability to handle more complex and heterogeneous data [14]. Among various approaches, implicit neural representation (INR) has received substantial attention in recent few years and successfully applied in medical imaging and graphics [15]. INR typically parameterizes a 3D surface structure or shape as continuous signed distance functions (SDFs) through a deep neural network, such as Multi-Layer Perceptrons (MLPs). Within this context, INR provides resolution-agnostic rendering and improved memory efficiency. After training, the 3D scene can be effectively represented by a straightforward MLP, with the flexibility to re-generate the mesh at varying resolutions during the reference stage.

However, the application of INR to freehand 3D US for continuous surface reconstruction is still missing. There are two main challenges in 3D freehand US to achieve high-quality surface reconstruction using deep learning. 1) Only the boundary of the target structure in 2D segmentation mask cannot accurately reflect the actual smooth surface because of the low signal-to-noise ratio (SNR) and poor connectivity in US images. 2) Different anatomical structures have different geometric priors, and, it's difficult to acquire sufficient ground truth volumes or templates to supervise the training stage for 3D surface reconstruction.

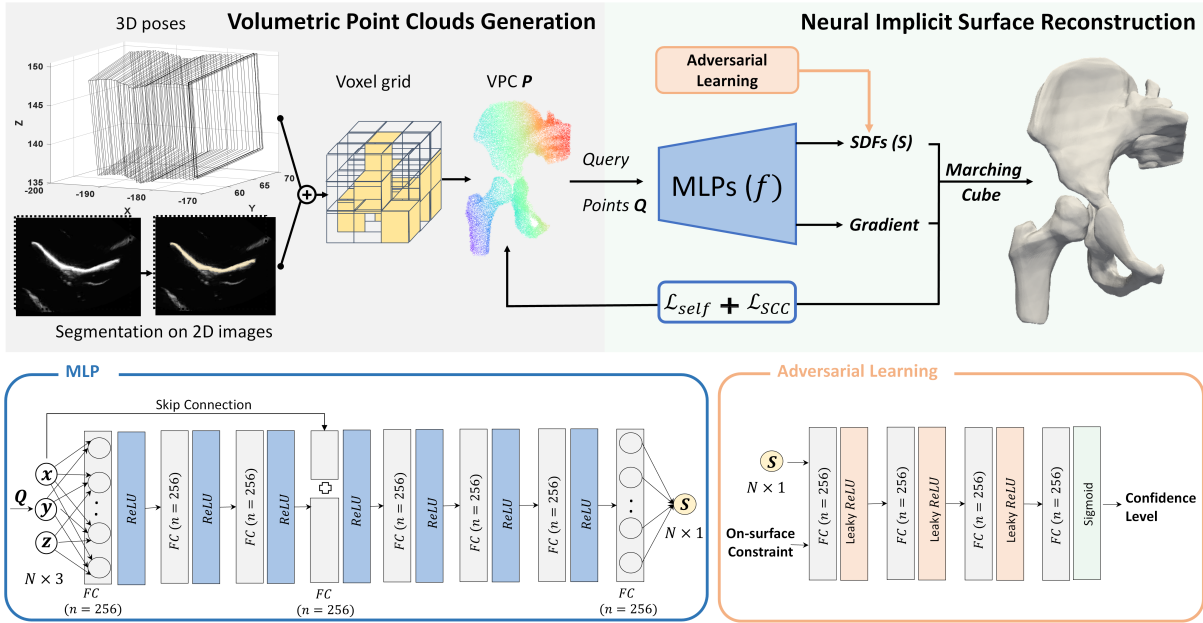


Fig. 1. Overview of the proposed neural implicit surface reconstruction method from the volumetric point clouds (VPC). The VPC P is first extracted from freehand 3D US data after the segmentation. A series of query points Q are then sampled around P and fed into the neural network for learning of Signed Distance Functions (SDFs, denoted as s). The final mesh file is generated using the Marching Cube algorithm via the predicted SDFs. The blue block at the bottom left depicts the MLPs neural network with eight fully connected layers (FC) and ReLU functions, and the orange block at the bottom right represents the on-surface constraint with adversarial learning.

B. Related works

1) *Traditional Surface Reconstruction in 3D Ultrasound*: Traditional surface reconstruction methods in 3D US can be simply classified into direct extraction and indirect segmentation. Zhang et al. [16] propose to directly extract the surface from freehand 3D US B-scans using the ISO-Surface after approximating a radial basis function across the pixels in 2D transverse images [17]. Nguyen et al. [13] first segments and digitizes the contours of target from the transverse B-mode images in the reconstructed US volume. The Bézier-spline function is then used to smooth and interpolate the contours to form a high-quality triangle mesh. Kerr et al. [18] adopts a column-wise thresholding method to segment the bony surface of each image as a point cloud from ultrasonic synthetic aperture images. The surface mesh is directly produced by the point clouds using a wrapping algorithm.

2) *DL-based 3D Surface Reconstruction in Medical Imaging*: Recent advances in DL-based 3D surface reconstruction methods have shown the promising results in radiographs, computerized tomography (CT), magnetic resonance image (MRI) and 3D echocardiography. Nakao et al. [19] combines the convolutional neural network and graph convolutional network to reconstruct 3D liver surface from a single 2D radiograph. Wickramasinghe et al. [20] develop the strategies for joint segmentation and

surface reconstruction to facilitate end-to-end training, converting the input CT volume directly to the output meshes. Ma et al. [21] propose a geometric learning framework to effectively reconstruct the cortical surface from brain MRI scans by a diffeomorphic flow and fast topology correction. Laumer et al. [22] develops a weakly supervised auto-encoder architecture to generate a 4D shape mesh for echocardiography from sequences of 2D mesh videos.

3) *Neural Implicit Surface Reconstruction*: The concept of INR has been widely applied in different medical imaging modalities, including MRI slice-to-volume reconstruction [23], CT limited-view reconstruction [24], freehand 3D US volume or sensorless reconstruction [25], [26]. In particular, the development of the INR of an SDF has emerged as a primary choice for the current neural implicit surface reconstruction from point clouds. Park et al. [27] proposes DeepSDF, an auto-decoder architecture, to learn an SDF in continuous space with the latent code by given ground truth signed distance values. Baorui et al. [28] further demonstrates the feasibility of SDFs to learn the 3D shape from surface point clouds using a Neural-pull operation without extra ground truth signed distance values, point cloud normal or occupancy value. Inspired by DeepSDF, Cruz et al. [29] introduces DeepCSR for the MRI cortical surface reconstruction from the points in a continuous brain template coordinate system. Sander et al. [30] trains the same auto-decoder architecture to complete the high-resolution 3D left ventricle shape from the sparse views of cardiac MRI (CMRI). Furthermore, Wiesner et al. [31] optimizes the auto-decoder in the spatial and temporal domain simultaneously to learn the shape of living cells from microscopy. The learned latent space is conditioned by a $SO(3)$ -equivariant to enforce rotational independence.

C. Contribution

In this paper, in order to handle the above issues mentioned in Section I-A, we propose an efficient online learning network to predict the SDFs for the implicit surface representation directly from freehand 3D US point clouds data. Instead of only considering the segmentation boundary, the whole segmentation masks and their locations are transformed into a 3D volumetric point clouds as the input. Our target is to use the neural network to overfit the underlying geometric surface in the point clouds as the continuous SDFs to avoid the disturbance of noise. Specifically, the 3D query points are sampled around the point clouds, and fed into the network to learn the SDFs between query points and point clouds using a self-supervised loss introduced by [28].

There are three primary contributions in this paper: 1) To the best of our knowledge, this is the first attempt to introduce an online neural implicit surface reconstruction method to take the 3D freehand US volumetric point cloud as input and learn the SDFs to reconstruct the surface of the medical anatomical structures effectively. The proposed method can learn the 3D continuous structures from individual input subject without the need for additional ground truth training data or post-processing. 2) We introduce two geometric constraints, sign consistency constraint and on-surface constraint in accordance with the adversarial learning strategy, aimed at enhancing surface reconstruction accuracy. 3) We conduct extensive experiments to assess the effectiveness of our approach using the six anthropomorphic phantoms with distinct medical shapes and seventeen *in vivo* carotid artery datasets acquired by three freehand 3D US imaging systems. The results demonstrate that the proposed method is competitive with current methods to highlight our advantages.

II. MATERIALS AND METHODS

A. Overview

The proposed method consists of two key components: the volumetric point cloud generation and the neural implicit surface reconstruction. In addition, two geometric constraints, including sign consistency constraint (SCC) and on-surface constraint with adversarial learning (OSC-ADL), are designed to ensure superior reconstruction quality.

As shown in Fig. 1, given a sequence of 2D transverse images with associated 3D freehand poses, the coordinates of 2D segmented masks are transformed into a 3D point cloud \mathbf{P} in the tracking space. The query points \mathbf{Q} are then sampled around \mathbf{P} as the input of MLPs network. The SDFs between \mathbf{Q} and the underlying surface described by \mathbf{P} are then progressively learned by the neural network, guided by geometric constraints in a self-supervised manner. The triangle mesh is ultimately produced by the Marching Cube algorithm using the predicted SDFs [32].

B. Volumetric Point Clouds Generation

The point cloud is an effective expression of medical data to record the implicit geometric information [33]. In this section, each 2D pixel \mathbf{v}_s in the segmented mask space is first transformed into the tracking space, \mathbf{v}_t [34],

$$\mathbf{v}_t = M_t M_c \mathbf{v}_s \quad (1)$$

where $\mathbf{v}_s = [x_s, y_s, 0, 1]^T$ and $\mathbf{v}_t = [x_t, y_t, z_t, 1]^T$ are in the homogeneous coordinate representation, M_c and M_t are the 4×4 calibration and tracking matrices from the freehand 3D US system, respectively.

These 3D points \mathbf{v}_t are then spatially discretized into voxel grids to acquire the volumetric point cloud $\mathbf{P} = \{\mathbf{p}_i, i = 1 \dots N\}$ for the uniform density distribution and smaller memory usage [35], [18]. For each \mathbf{p}_i in \mathbf{P} , a set of 3D query points $\mathbf{Q} = \{\mathbf{q}_{ij}, j = 1 \dots l\}$ are randomly sampled around it following Gaussian distribution $(0, \delta)$ [28]. Here, δ is selected as the

Euclidean distance between p_i and its k -th nearest neighbor, N and l are the total number of 3D point cloud and the query points, respectively.

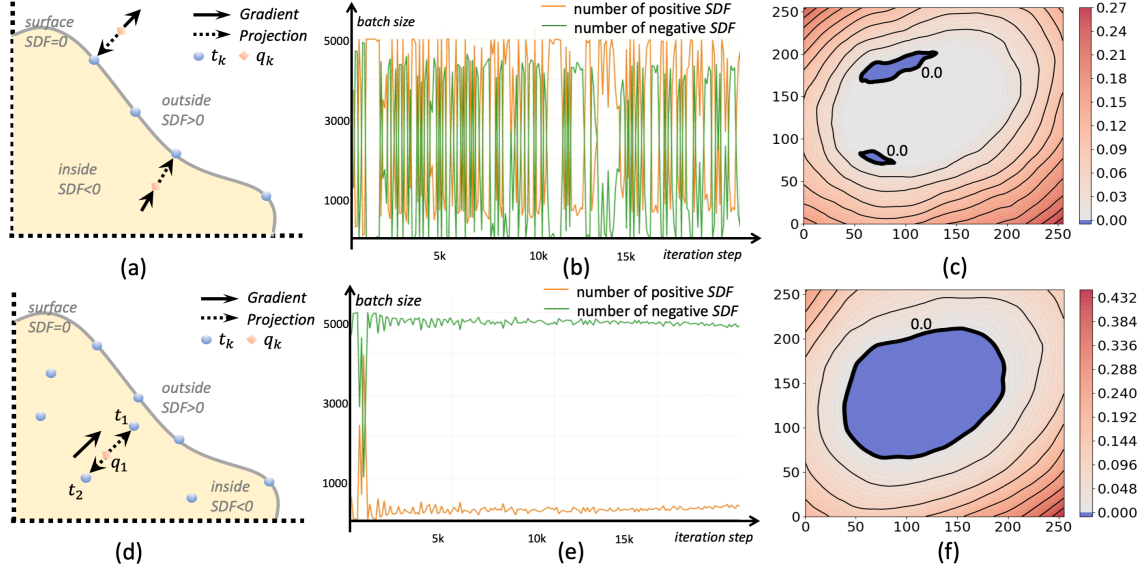


Fig. 2. The 2D demonstration of sign consistency constraint from the carotid sample. (a) and (d) the projection near the surface and inside the surface. (b) and (e) the plot of the number of SDF learned from distance loss only and with SCC loss. (c) and (f) the level-sets of SDF learned from distance loss only and with SCC loss. The blue region and red region indicate the negative area (inside) and positive area (outside), respectively. The bold black contour outlines the zero-level-set of surface.

C. Neural Implicit Surface Reconstruction

1) *Self-supervised Learning of SDFs from Point Clouds*: The SDFs are a crucial continuous representation to describe the 3D shape by dividing the surface as exterior (positive), on-surface (zero) and interior (negative) [36], [27]. In this paper, we indicate the SDFs through learning the signed distances between the surface represented by point cloud \mathbf{P} and query points \mathbf{Q} .

$$SDF(q_{ij}, p_i) = \{s \in \mathbb{R} \mid q_{ij} \in \mathbf{Q}, p_i \in \mathbf{P}\} \quad (2)$$

where $p_i = [x_i, y_i, z_i]$ is the 3D point in volumetric point cloud, $q_{ij} = [x_{ij}, y_{ij}, z_{ij}]$ is the sampled query point around p_i , and s is the predicted signed distance between \mathbf{Q} and the surface represented by \mathbf{P} . The underlying surface boundary is depicted by a zero-level-set of $SDF(*) = 0$, which can be easily used to extract mesh by Marching Cube.

To simplify the notation, each query point is re-denoted as $\{q_k, k = 1 \dots l\}$. Then, for each q_k , we find its nearest neighbor point $t_k \in \mathbf{P}$ under the Euclidean distance for the calculation of self-supervised loss. As described in Fig. 1, an MLPs neural network f is trained to learn the SDF value and gradient of a given query point q_k in \mathbf{Q} . The query point is then projected along or against the learned gradient to its nearest point t_k using the predicted SDF value. The projection process is illustrated in Fig. 2(a) and formulated as the below equation.

$$q_k' = q_k - f(q_k) \times \frac{\nabla f(q_k)}{\|\nabla f(q_k)\|_2} \quad (3)$$

where $f(q_k)$, also denoted as s , is the predicted signed distance from the network, $\nabla f(q_k) / \|\nabla f(q_k)\|$ is the normalized gradient of the network, indicating the direction in 3D space where the signed distance increases most rapidly.

Following Neural-pull [28], we minimize the self-supervised L2-distance loss to optimize the projected q_k' approaching its nearest neighbor $t_k \in \mathbf{P}$.

$$\mathcal{L}_{self} = \frac{1}{K} \sum_{k \in [1, K]} \|q_k' - t_k\|_2^2 \quad (4)$$

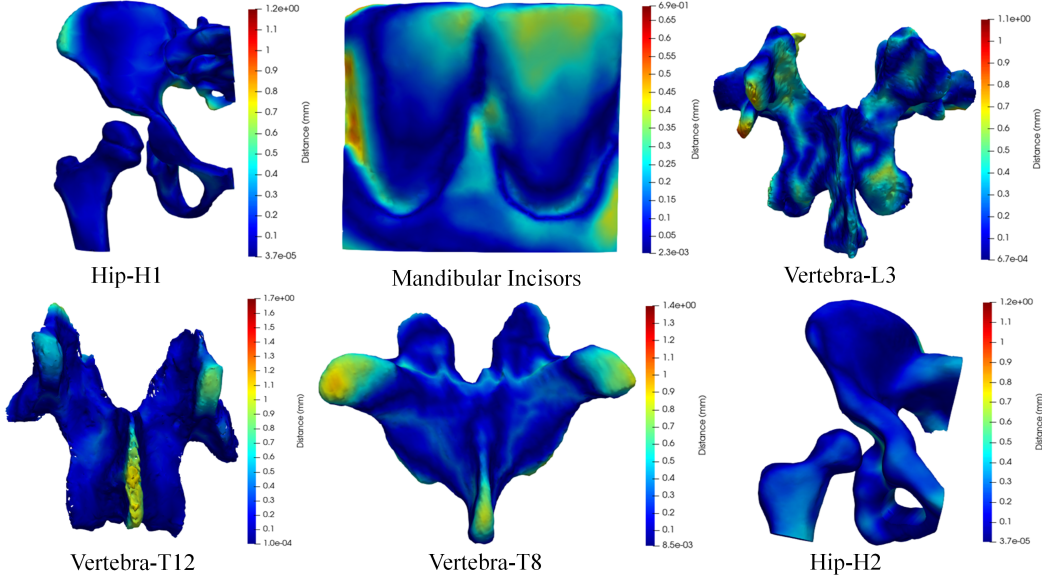


Fig. 3. Reconstructed surfaces with colormap indicating the distance to the pseudo-ground-truth surfaces of CAD models from six phantoms.

2) *Sign Consistency Constraint for Volumetric Point Clouds*: In order to learn a better underlying surface, our input is the whole mask instead of the boundary. However, as proved in [36], only using Eq. (4) to supervise the training has no explicit penalties for the predicted wrong sign when the query point is close to the surface. This limitation will lead the network to converge to an unstable status, especially inside the mask.

A simple 2D case is illustrated in Fig. 2(d), t_1 and t_2 are two points inside the surface, q_1 is the corresponding nearest query point around t_1 and t_2 , respectively. Following Eq. (3), the network will predict a negative sign distance to project q_1 to t_1 along the direction of the gradient and minimize the loss Eq. (4). However, in the next training batch, t_2 , as the opposite direction of t_1 , will make the network try to change the sign to minimize Eq. (4) against the gradient. Obviously, this will lead the predicted sign inside the mask to be in a chaotic state. As shown the Fig. 2(b) and Fig. 2(c), the number of positive signs and negative signs varies wildly at each iteration and the zeros-level-set boundary disappears.

To address this problem, we introduce a direction loss as SCC to balance the distance loss by the following formula,

$$L_{SCC} = \frac{1}{K} \sum_{k \in [1, K]} 1 - \cos \left(\nabla f(q_k), \frac{(q'_k - t_k)}{\|q'_k - t_k\|_2} \right) \quad (5)$$

In this case, even though the distance loss is small, the constraint on the projection path will force the network to change the direction of the gradient in the next training batch, but not the sign. Fig. 2(e) and Fig. 2(f) demonstrate that the predicted positive and negative values are quickly stabilized after using the proposed SCC, and the zeros-level-set boundary is still well-preserved.

3) *On-surface Constraint with Adversarial Learning*: On-surface prior is another important geometric constraint to improve the surface reconstruction, especially in dealing with complex medical structures. Ideally, the network will converge to the actual surface boundary, allowing us to accurately distinguish the inside and outside of a structure by $SDF = 0$ on the surface. However, lacking the on-surface prior can result in the inaccurate or even wrong prediction in complex cases, such as the shapes with polygonal holes.

To leverage more information, we propose encoding the OSC-ADL to enforce the network to learn a more compact shape. The ADL module, consisting of four fully connected MLPs and Leaky ReLU activation functions, serves as an adversarial discriminator. Specifically, the anatomical structure boundary corresponds to a prior SDF of 0, representing the on-surface constraint. The adversarial discriminator distinguishes between the SDF values predicted by the network f and the on-surface prior values. It quantifies the confidence level between the network's SDF predictions and the on-surface constraint by employing a sigmoid layer. Through this adversarial learning process, the network's SDF predictions are iteratively guided to accurately represent the surface boundary of anatomical structures, ultimately enhancing the precision of our surface reconstruction methodology.

D. Loss Functions

Overall, the entire network is optimized end-to-end by minimizing \mathcal{L}_G and \mathcal{L}_D in an adversarial manner during the training stage. The \mathcal{L}_G is the adversarial generator loss to train the MLPs with self-supervised loss and SCC loss, and the \mathcal{L}_D is the

TABLE I

PERFORMANCE COMPARISON OF OUR APPROACH WITH THE BASELINE METHOD ON THE SIX PHANTOM DATASETS AT 1.5×10^4 ITERATIONS (MEAN \pm STANDARD DEVIATION). A LOWER DISTANCE (\downarrow) MEANS A BETTER RESULT.

Phantom Datasets	Chamfer distance (mm) \downarrow		Hausdorff distance (mm) \downarrow		Average absolute distance (mm) \downarrow	
	Neural-pull	Proposed	Neural-pull	Proposed	Neural-pull	Proposed
H1	3.03 \pm 0.30	1.04 \pm 0.10	3.18 \pm 0.51	1.28 \pm 0.16	3.99 \pm 0.14	1.86 \pm 0.10
Mandibular	0.23 \pm 0.05	0.12 \pm 0.07	0.83 \pm 0.12	0.69 \pm 0.11	0.19 \pm 0.45	0.18 \pm 0.07
L3	3.48 \pm 0.83	1.05 \pm 0.52	3.52 \pm 0.62	1.14 \pm 0.40	3.38 \pm 0.61	1.18 \pm 0.57
T12	4.17 \pm 1.53	1.09 \pm 0.99	4.82 \pm 1.14	1.68 \pm 0.25	4.36 \pm 0.92	1.16 \pm 0.57
T8	3.35 \pm 0.53	1.21 \pm 0.99	3.66 \pm 0.48	1.41 \pm 0.86	3.66 \pm 0.77	1.58 \pm 0.53
H2	2.52 \pm 1.40	1.04 \pm 0.13	2.27 \pm 1.58	1.17 \pm 0.29	2.62 \pm 1.42	1.15 \pm 0.18

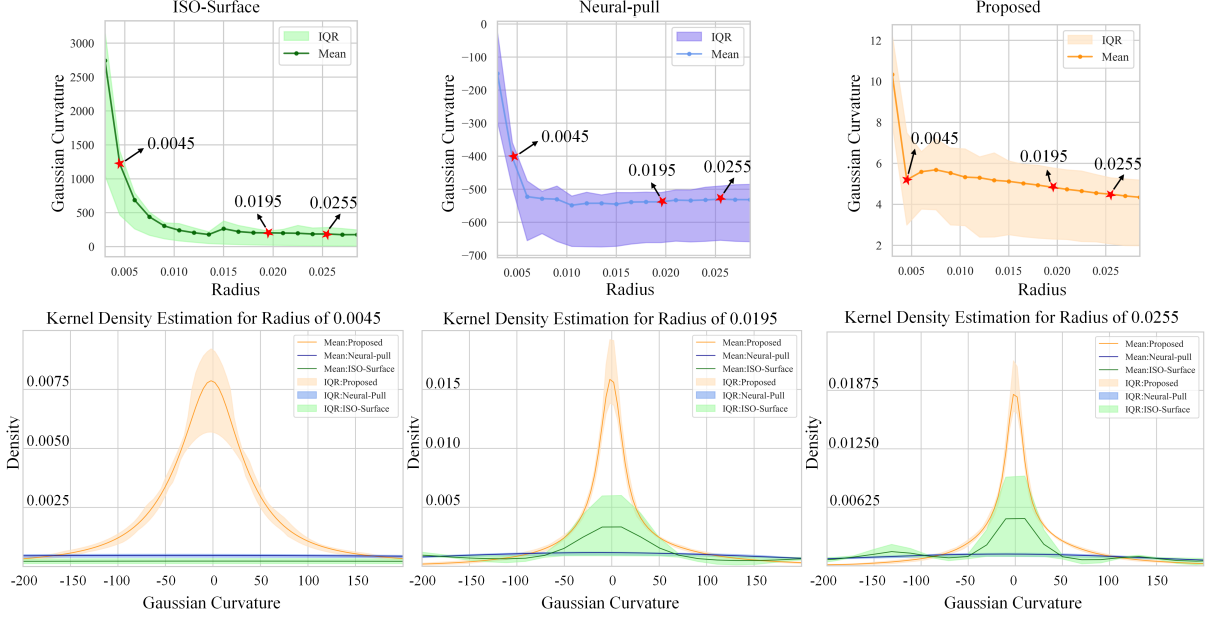


Fig. 4. Quantitative evaluation of smoothness of reconstructed meshes from seventeen *in vivo* carotid artery datasets. The plots show descriptive statistics (mean and interquartile range) of three methods based on Gaussian curvature (top) and kernel density (bottom). For the density of three methods, the higher amplitude of the Gaussian curve, the smoother it is.

adversarial discriminator loss. Here, we directly minimize the least-squared adversarial loss [37] between the predicted SDF values and zero scalar field's value:

$$\mathcal{L}_G = \lambda_{self} \mathcal{L}_{self} + \lambda_{scc} \mathcal{L}_{SCC} + \lambda_G \frac{1}{2} [D(\mathbf{s}) - 1]^2 \quad (6)$$

$$\mathcal{L}_D = \frac{1}{2} [D(\mathbf{s})^2 + (D(\mathbf{s}') - 1)^2] \quad (7)$$

where, λ_{self} , λ_{scc} and λ_G are the weights, \mathbf{G} , \mathbf{D} are optimized alternatively during the training process, \mathbf{s} and \mathbf{s}' denotes the MLPs' output and zero scalar field's value (on-surface constraint), respectively.

III. EXPERIMENTS

A. Datasets

To assess the generalizability and robustness of the proposed method, a total of 23 distinct datasets are utilized for our experimental analysis. These datasets are acquired from three commonly used freehand 3D US imaging systems, as detailed in references [38], [39], [40]. We divide the datasets into phantom datasets and *in vivo* datasets. The phantom datasets have six anthropomorphic phantoms with computer-aided designed (CAD) models, including three vertebrae (L3, T12, T8), two hips (H1, H2), and a mandibular incisors phantom. These phantoms are used as the pseudo-ground-truth for the evaluation of network performance. Additionally, the *in vivo* datasets consisting of seventeen carotid artery shapes are collected from local hospital and used for both qualitative and quantitative analysis. This study has been approved by the relevant local research ethics committees. For comprehensive specifications of these data acquisition systems and datasets, please see Appendix.

B. Implementation Details

During the training phase, all the extracted point clouds are randomly down-sampled under 7×10^4 and 25 query points are sampled for each point $p \in P$. The weights of network are initialized following [28]. We train the network for 2×10^4 iterations using the Adam optimizer with a learning rate of 0.001 and a momentum of 0.9. The batch size, λ_{scc} and λ_G are set as 5000, 0.01 and 0.01, respectively. Our network is implemented using Pytorch and trained on a single NVIDIA RTX 3070 GPU with 8 GB memory. During the reference, we set the threshold of Marching Cube to 0 and resolution to $256 \times 256 \times 256$ in a normalized range of $\{-1,1\}$ to generate the mesh based on the predicted SDFs.

C. Evaluation on Phantom Datasets

We benchmark our results with the established baseline method in computer vision, Neural-pull, since we are the first to introduce the self-supervised strategy for the surface reconstruction in freehand 3D US. To evaluate the geometric accuracy of the reconstruction, we employ three metrics, L2-Chamfer Distance (CD), Hausdorff Distance (HD), and Average absolute distance (AB). These distances quantify the discrepancies between the reconstructed surfaces and their corresponding CAD models. For a robust assessment, we randomly sample 80% of points from both the reconstructed surface meshes and CAD models for each phantom to participate in the distance calculation. As shown in Table I, our method demonstrates consistent superiority over the Neural-pull method across all three distance metrics at the 1.5×10^4 iterations.

Notably, we observe a substantial average decrease of 67% in CD, 60% in HD, and 61% in AB for all the phantoms, indicating the superior accuracy of the proposed method in matching corresponding points on the ground truth surfaces. Specifically, for phantom H1, H2, T8, T12 and L3 used with the same electromagnetic positioning device, the mean and standard deviation values of the distance metrics from our method and Neural-pull are found to be 1.08 ± 0.06 vs. 3.31 ± 0.42 mm for CD, 1.33 ± 0.19 vs. 3.49 ± 0.82 mm for HD, 1.39 ± 0.29 vs. 3.60 ± 0.60 mm for AB. Furthermore, the results of AB for each phantom using our method closely approximate to the imaging resolution of the data acquisition system, indicating high fidelity in surface reconstruction.

We also evaluate the point-to-point distance between our reconstructed results with the corresponding CAD models using 3D Slicer (<https://www.slicer.org/>). The superimposed differences are encoded in a colormap from blue (low discrepancy) to red (high discrepancy). As illustrated in Fig. 3, our proposed method achieves the remarkable accuracy of the geometric shape of each distinct phantom model.

TABLE II
TOPOLOGICAL MEASURES AND SIMILARITY COMPUTATION FOR THREE METHODS OVER SEVENTEEN IN VIVO CAROTID ARTERY DATASETS.

Methods	Connected Components	Genus	IoU	Dice
Neural-pull	29.3 ± 14.8	79.7 ± 34.7	\	\
ISO-Surface	1.0	0.0	0.84 ± 0.04	0.90 ± 0.03
Proposed	1.0	0.0	0.86 ± 0.04	0.92 ± 0.02

D. Evaluation on In Vivo Datasets

In this subsection, we compare the proposed method with Neural-pull and ISO-surface on the *in vivo* carotid artery datasets both quantitatively and qualitatively. Since there is no 3D ground truth shape available for these datasets, we first geometrically evaluate the completeness and smoothness of reconstructed meshes, including topological measures, Gaussian curvature computation and kernel density estimation. An ideal reconstruction of a closed carotid surface should have only one connected components and zero genus [41]. However, as shown in Table II, the baseline method Neural-pull fails to maintain the shape integrity, resulting in a high number of connected components (29.3 ± 14.8) and genus (79.7 ± 34.7), in contrast to our method and ISO-Surface. Fig. 4 shows the descriptive statistics (mean and interquartile range) of Gaussian curvature computation and the associated kernel density estimation on the normalized, reconstructed mesh of each carotid artery shape. The top plots illustrate the variation of Gaussian curvature across different radii. We then choose one radius (0.0045) and two radii (0.0195, 0.0255) before and after the stabilization of Gaussian curvature for density estimation as shown in the bottom plots. In comparison to the other two reconstruction methods, our proposed INR-based method shows superior ability in predicting more continuous and smooth structures without the resolution limitations. This is evidenced by the observation of maximum Gaussian probability density close to zero and minimal variation in the interquartile range.

To verify the similarity between the predicted surfaces and the actual vessel shape, we further calculate the Jaccard index (intersection over union / IoU) and Dice coefficient score for the predicted vessel contour versus the reference contour following [22]. The predicted vessel contour is individually resliced along the longitudinal direction at a specific degree from the reconstructed mesh, while the reference contour is derived from the expert labels collected from the clinical equipment. Further details on the reslicing operation can be found in [39]. The results, reported in columns 3 and 4 of Table II, show that

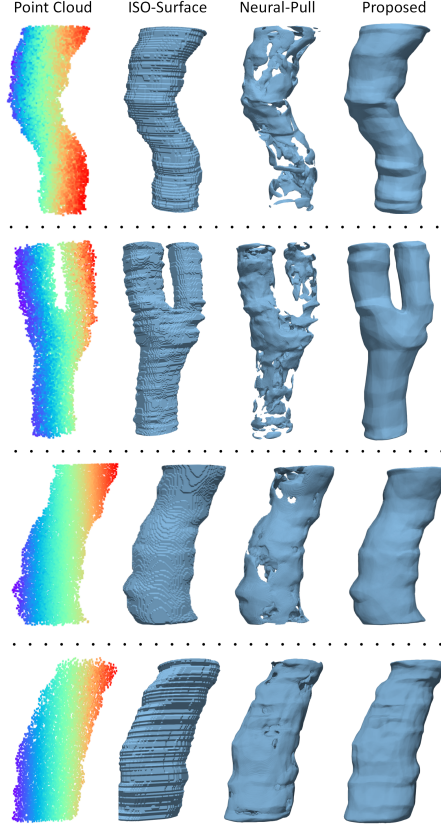


Fig. 5. Four examples of reconstructed meshes from *in vivo* carotid artery datasets at 1.5×10^4 iterations. The blue-to-red color in point cloud illustrates the directional changes from left to right.

TABLE III
ABLATION STUDIES ON THE EFFECTIVENESS OF THE PROPOSED GEOMETRIC CONSTRAINTS USING TWO HIP PHANTOMS AT 1.5×10^4 AND 2.0×10^4 ITERATIONS.

Methods	1.5×10^4		2.0×10^4	
	CD (mm)	HD (mm)	CD (mm)	HD (mm)
H1 phantom model				
Baseline	3.03 ± 0.30	3.18 ± 0.51	3.56 ± 2.14	4.12 ± 2.14
SCC	1.20 ± 0.23	1.41 ± 0.20	1.18 ± 0.23	1.34 ± 0.23
OSC-ADL	1.60 ± 0.30	2.65 ± 0.26	1.37 ± 0.29	2.25 ± 0.25
Proposed	1.04 ± 0.10	1.28 ± 0.16	1.12 ± 0.10	1.12 ± 0.20
H2 phantom model				
Baseline	2.52 ± 1.40	2.27 ± 1.58	3.02 ± 3.46	3.65 ± 3.34
SCC	1.33 ± 0.24	1.39 ± 0.32	1.41 ± 0.33	1.99 ± 0.37
OSC-ADL	1.75 ± 0.32	1.99 ± 0.38	2.14 ± 0.68	2.20 ± 0.94
Proposed	1.04 ± 0.13	1.17 ± 0.29	1.34 ± 0.20	1.95 ± 0.37

the Neural-pull method can not calculate the similarity due to the incomplete structures it produced. Although the mesh of ISO-Surface method, generated from well-segmented masks, can naturally reflect the actual shape with a good overlap score, our method still achieves 2.83% higher IoU and 1.83% higher Dice than ISO-Surface.

We qualitatively present four examples of reconstructed meshes as well as the corresponding point clouds in Fig. 5. While the ISO-Surface is capable of generating accurate shapes, it is limited by the resolution and discontinuities. The Neural-pull method presents the advantage of smoothness through INR, yet it struggles to reach the actual surface boundary and loses integrity without geometric constraints. Overall, our proposed method demonstrates superior performance in both accuracy and visualization.

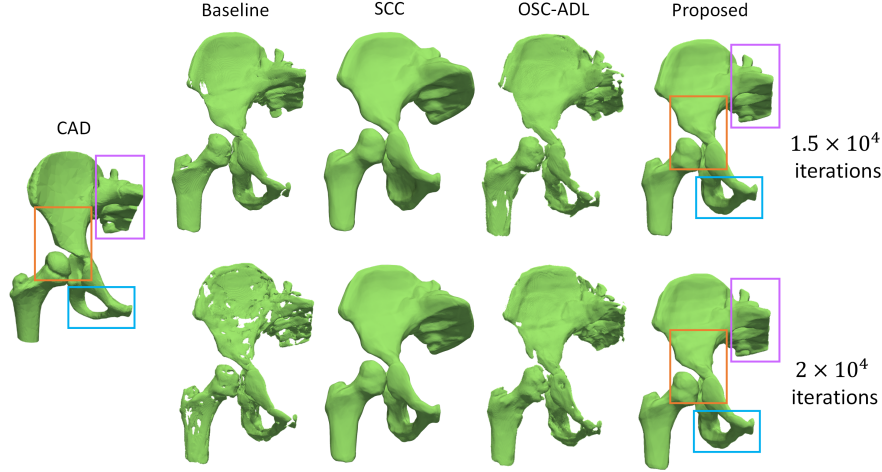


Fig. 6. Visualization of the ablation study on the H1 phantom for the validation of geometric constraints. The top and bottom plots are the reconstructed surface of baseline (Neural-pull), only SCC, only OSC-ADL and the proposed method at 1.5×10^4 and 2.0×10^4 iterations, respectively. The pseudo-ground-truth CAD model is shown on the left. Three colored boxes highlight the main differences.

E. Ablation Study

In this subsection, to investigate the capability of each module of the proposed method, we perform a comprehensive ablation study on the two hip phantoms, including the effectiveness of two geometric constraints and the performance of two input types. We train the online network for 2.0×10^4 iterations and compare the result of each module at 1.5×10^4 and 2.0×10^4 iterations.

1) *Validating the Effectiveness of Geometric Constraints*: The effectiveness of the proposed approach is attributed to the incorporation of two geometric constraints, SCC and OSC-ADL. We have individually evaluated their efficiency on the two hip phantom models by both qualitative and quantitative analysis. We chose the Neural-pull as the baseline method. And the ablation study is carried out by separately adding SCC or OSC-ADL to the baseline.

Table III reports the individual contribution of SCC and OSC-ADL to the enhancement of surface reconstruction performance. Compared with the baseline at 1.5×10^4 iterations, the SCC results improve 60% CD, 56% HD for H1 phantom and 47% CD, 39% HD for H2 phantom, respectively. The OSC-ADL results also demonstrate the decrease of 47% CD, 17% HD for H1 phantom and 31% CD, 12% HD for H2 phantom, respectively. Furthermore, the most significant improvements are observed when both constraints are jointly optimized in the proposed method, revealing a lower CD (66%), HD (60%) on H1 phantom and lower CD (59%), HD (48%) on H2 phantom, respectively. Besides, the proposed method can also improve the accuracy by decreasing 69% CD, 70% HD on H1 phantom and 56% CD, 47% HD on H2 phantom at 2.0×10^4 , respectively.

Fig. 6 shows an example of the ablation study conducted on the H1 phantom model. The baseline method presents the worst structures, showing the broken surface and imperfect shape, especially at the 2.0×10^4 iterations. The SCC loss illustrates the ability to reconstruct the overall shape at both iterations compared to the baseline. However, only using SCC fails to handle certain tough detailed structures at the 1.5×10^4 iterations, as indicated by the purple and blue boxes. The edge of the sacrum (purple) appears to be inflated and the obturator foramen at the bottom (blue) is filled. In contrast, the OSC-ADL module can recover the detailed structures, but lose the shape completeness due to the absence of SCC. This observation is also observed in Table III, where SCC exhibits a more substantial improvement in reconstruction accuracy than OSC-ADL, indicating a lower CD (22%) and HD (70%) for H1 and lower CD (35%) and HD (68%) for H2 at 1.5×10^4 iterations. By combining both constraints, our proposed method is able to effectively preserve all the anatomical structures at 1.5×10^4 and 2.0×10^4 iterations. The above results significantly demonstrate the ability of our method to realize high reconstruction quality and fast convergence speed.

2) *Comparing the Performance of Volumetric Point Cloud with Surface Point Cloud*: In this experiment, we investigate the network performance with different types of input data, including surface point cloud (SPC) and volumetric point cloud (VPC). The SPC data, which serves as the original input for Neural-pull, is extracted only from the segmented boundary. While the VPC data is generated from all the voxels within the segmentation masks. A visual contrastive analysis of two input types is shown on the right of Fig. 7. The VPC exhibits a dense aggregation of 3D points within the mask area, which provides enriched information for the underlying shape representation. Therefore, only using the SPC as the input will lead the network to produce a coarser local surface or even lose the integrity as opposed to the results using VPC. One possible reason is that unlike Lidar-generated point clouds in computer vision, US data is typically noisy. The differences are most apparent on the three highlight boxes. Our proposed method shows the advantage of representing continuity and completeness, particularly in achieving a smoother surface when using VPC, as indicated by the orange box in Fig. 7.

TABLE IV
 ABLATION STUDIES ON THE PERFORMANCE OF TWO INPUT DATA TYPES, SURFACE POINT CLOUD (S) VERSUS VOLUMETRIC POINT CLOUD (V), USING HIP PHANTOMS AT 1.5×10^4 AND 2.0×10^4 ITERATIONS.

Methods	1.5×10^4		2.0×10^4	
	CD (mm)	HD (mm)	CD (mm)	HD (mm)
H1 phantom model				
Baseline-S	14.04 ± 9.81	21.80 ± 9.21	14.01 ± 7.0	21.08 ± 9.15
Baseline-V	3.03 ± 0.30	3.18 ± 0.51	3.56 ± 2.14	4.12 ± 2.14
Proposed-S	1.16 ± 0.27	1.29 ± 0.15	1.14 ± 0.13	1.17 ± 0.21
Proposed-V	1.04 ± 0.10	1.28 ± 0.16	1.12 ± 0.10	1.12 ± 0.20
H2 phantom model				
Baseline-S	10.66 ± 8.17	26.14 ± 7.39	12.51 ± 16.21	26.68 ± 14.56
Baseline-V	2.52 ± 1.40	2.27 ± 1.58	3.02 ± 3.46	3.65 ± 3.34
Proposed-S	1.07 ± 0.95	1.17 ± 1.04	1.72 ± 0.49	2.13 ± 0.44
Proposed-V	1.04 ± 0.13	1.17 ± 0.29	1.34 ± 0.20	1.95 ± 0.37

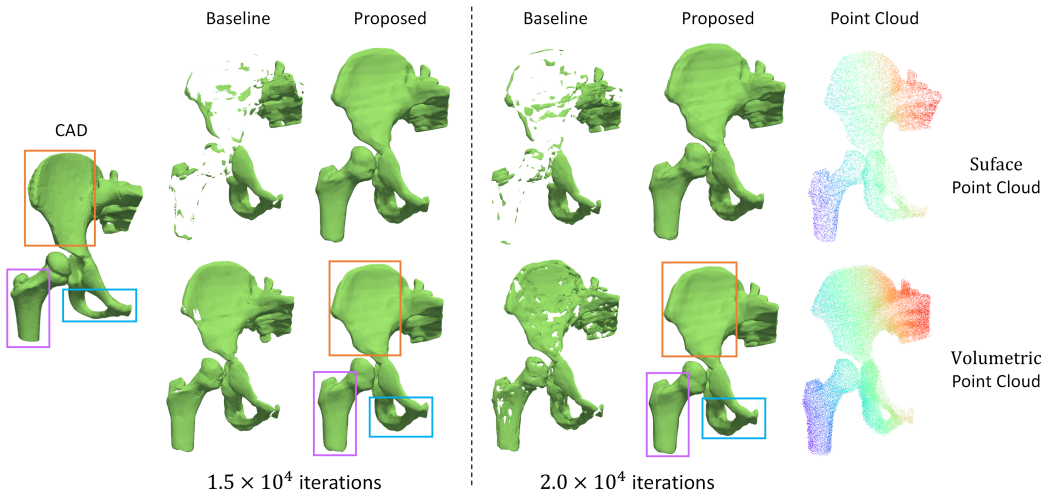


Fig. 7. Visualization of the ablation study on the H1 phantom for the comparison of different inputs. The results at 1.5×10^4 and 2.0×10^4 iterations are presented on the left block and right block. The top and bottom plots are the reconstructed surface of baseline (Neural-pull) and the proposed method using surface point cloud and volumetric point cloud, respectively. The pseudo-ground-truth CAD model is shown on the left. The blue-to-red color in point cloud indicates the directional changes from left to right. Three colored boxes highlight the main differences.

We also present quantitative assessment for two hip phantoms using CD and HD in Table IV. The numerical results align with the visual inspection in Fig. 7, with Neural-pull method showing that SPC input yields the highest CD and HD due to the vanishing reconstructed boundaries. The accuracy of Neural-pull is then improved by using VPC. For example, the CD and HD of H1 phantom are reduced from 14.04 ± 9.81 to 3.03 ± 0.30 and 21.80 ± 9.21 to 3.18 ± 0.51 at 1.5×10^4 iterations. In contrast, the performance of our method utilizing SPC or VPC is both significantly enhanced in comparison to Neural-pull and achieves the lowest discrepancy using VPC.

IV. DISCUSSION AND CONCLUSION

We have developed a novel DL-based approach, incorporating geometric constraints, to learn SDFs for the neural implicit surface reconstruction of freehand 3D US volumetric point clouds. The proposed constraints allow us to effectively minimize the sign variations and reconstruction errors during the training. The results demonstrate our method is highly effective at reconstructing the 3D surface of medical anatomical structures with complex structures and incomplete surfaces, outperforming the state-of-the-art method in qualitative and quantitative assessments. One positive advantage of our approach, unlike other DL-based methods, the training process does not require ground-truth data and is able to reconstruct the 3D surface within 5 minutes using a single GPU card. The promising results have the potential to advance the application of freehand 3D US in medical augmented reality, surgical navigation and computer-assisted interventions.

Although our method proves to be valuable for the current situation, it's important to acknowledge some limitations. First, it's difficult to directly validate the reconstruction accuracy of *in vivo* datasets due to the unavailability of ground truth shapes for freehand 3D US. Consequently, we employ the geometric measures and expert labels for the indirect evaluation. Second, although the reconstruction time for each dataset is already under five minutes using a single GPU card, the reconstruction

TABLE V
APPENDIX I: OVERVIEW OF THE GRID SIZE, DATASETS AND DATA ACQUISITION SYSTEMS IN THE EXPERIMENTS.

Datasets (Number)	Shape	US Transducer	Pixel Resolution and Frequency	Tracking Device	Tracking Resolution	Grid Size
Phantoms (6)	Hip [38] (H1,H2)	Clarius C3HD Canada	0.2 mm up to 5MHz	Polhemus G4 USA	2 mm	0.5 mm
	Vertebrae (T8, T12, L3)	In-lab custom transducer	0.015 mm up to 23MHz	OptiTrack Flex13 USA	0.2 mm	0.1 mm
in vivo (17)	Carotid Artery [39]	Clarius L7HD Canada	0.075 mm up to 10MHz	Polhemus G4 USA	2 mm	0.2 mm

speed can be further improved. For a simple implementation, our current approach considers the entire segmentation mask as a volumetric input, which increases the memory usage and computational cost. For future work, it would be helpful to investigate resampling strategies to reduce the use of points in the central region of the mask to further accelerate the reconstruction.

APPENDIX I

Table V summarizes the spacing size of the voxel grid, datasets and detailed technical parameters of used freehand 3D US data acquisition systems. The spacing size of the voxel grid is set according to the pixel resolution of ultrasound transducer and tracking resolution based on our previous works.

REFERENCES

- [1] M. Jiang and B. Chiu, "A dual-stream centerline-guided network for segmentation of the common and internal carotid arteries from 3D ultrasound images," *IEEE Transactions on Medical Imaging*, pp. 1–1, 2023.
- [2] X. Yang, H. Dou, R. Huang, W. Xue, Y. Huang, J. Qian, Y. Zhang, H. Luo, H. Guo, T. Wang, Y. Xiong, and D. Ni, "Agent With Warm Start and Adaptive Dynamic Termination for Plane Localization in 3D Ultrasound," *IEEE Transactions on Medical Imaging*, vol. 40, no. 7, pp. 1950–1961, Jul. 2021.
- [3] R. W. Prager, U. Z. Ijaz, A. H. Gee, and G. M. Treece, "Three-dimensional ultrasound imaging," *Proceedings of the Institution of Mechanical Engineers, Part H: Journal of Engineering in Medicine*, vol. 224, no. 2, pp. 193–223, Feb. 2010.
- [4] M. Luo, X. Yang, H. Wang, H. Dou, X. Hu, Y. Huang, N. Ravikumar, S. Xu, Y. Zhang, Y. Xiong, W. Xue, A. F. Frangi, D. Ni, and L. Sun, "RecON: Online learning for sensorless freehand 3D ultrasound reconstruction," *Medical Image Analysis*, vol. 87, p. 102810, Jul. 2023.
- [5] R. Rohling, A. Gee, and L. Berman, "A comparison of freehand three-dimensional ultrasound reconstruction techniques," *Medical Image Analysis*, vol. 3, no. 4, pp. 339–359, Dec. 1999.
- [6] M. H. Mozaffari and W.-S. Lee, "Freehand 3-D Ultrasound Imaging: A Systematic Review," *Ultrasound in Medicine & Biology*, vol. 43, no. 10, pp. 2099–2124, Oct. 2017.
- [7] Q. Huang and Z. Zeng, "A Review on Real-Time 3D Ultrasound Imaging Technology," *BioMed Research International*, vol. 2017, pp. 1–20, 2017.
- [8] G. Chen, J. Qin, B. B. Amor, W. Zhou, H. Dai, T. Zhou, H. Huang, and L. Shao, "Automatic Detection of Tooth-Gingiva Trim Lines on Dental Surfaces," *IEEE Transactions on Medical Imaging*, vol. 42, no. 11, pp. 3194–3204, Nov. 2023.
- [9] H. Zhou and J. Jagadeesan, "Real-Time Dense Reconstruction of Tissue Surface From Stereo Optical Video," *IEEE Transactions on Medical Imaging*, vol. 39, no. 2, pp. 400–412, Feb. 2020.
- [10] R. Palomar, F. A. Cheikh, B. Edwin, A. Beghdadhi, and O. J. Elle, "Surface reconstruction for planning and navigation of liver resections," *Computerized Medical Imaging and Graphics*, vol. 53, pp. 30–42, Oct. 2016.
- [11] F. Mohamed and C. V. Siang, *A Survey on 3D Ultrasound Reconstruction Techniques*. IntechOpen, Apr. 2019.
- [12] G. Treece, R. Prager, and A. Gee, "Regularised marching tetrahedra: Improved iso-surface extraction," *Computers & Graphics*, vol. 23, no. 4, pp. 583–598, Aug. 1999.
- [13] D. V. Nguyen, Q. N. Vo, L. H. Le, and E. H. M. Lou, "Validation of 3D surface reconstruction of vertebrae and spinal column using 3D ultrasound data – A pilot study," *Medical Engineering & Physics*, vol. 37, no. 2, pp. 239–244, Feb. 2015.
- [14] A. Farshian, M. Götz, G. Cavallaro, C. Debus, M. Nießner, J. A. Benediktsson, and A. Streit, "Deep-Learning-Based 3-D Surface Reconstruction—A Survey," *Proceedings of the IEEE*, vol. 111, no. 11, pp. 1464–1501, Nov. 2023.
- [15] A. Molaie, A. Aminimehr, A. Tavakoli, A. Kazerouni, B. Azad, R. Azad, and D. Merhof, "Implicit Neural Representation in Medical Imaging: A Comparative Survey," in *Proceedings of the IEEE/CVF International Conference on Computer Vision*, 2023, pp. 2381–2391.
- [16] W. Y. Zhang, R. N. Rohling, and D. K. Pai, "Surface extraction with a three-dimensional freehand ultrasound system," *Ultrasound in Medicine & Biology*, vol. 30, no. 11, pp. 1461–1473, Nov. 2004.
- [17] Y. Zhang, R. Rohling, and D. Pai, "Direct surface extraction from 3D freehand ultrasound images," in *IEEE Visualization, 2002. VIS 2002.*, Oct. 2002, pp. 45–52.
- [18] W. Kerr, P. Rowe, and S. G. Pierce, "Accurate 3D reconstruction of bony surfaces using ultrasonic synthetic aperture techniques for robotic knee arthroplasty," *Computerized Medical Imaging and Graphics*, vol. 58, pp. 23–32, Jun. 2017.
- [19] M. Nakao, F. Tong, M. Nakamura, and T. Matsuda, "Image-to-Graph Convolutional Network for Deformable Shape Reconstruction from a Single Projection Image," in *Medical Image Computing and Computer Assisted Intervention – MICCAI 2021*, ser. Lecture Notes in Computer Science, M. de Bruijne, P. C. Cattin, S. Cotin, N. Padoy, S. Speidel, Y. Zheng, and C. Essert, Eds. Cham: Springer International Publishing, 2021, pp. 259–268.
- [20] U. Wickramasinghe, E. Remelli, G. Knott, and P. Fua, "Voxel2Mesh: 3D Mesh Model Generation from Volumetric Data," in *Medical Image Computing and Computer Assisted Intervention – MICCAI 2020*, ser. Lecture Notes in Computer Science, A. L. Martel, P. Abolmaesumi, D. Stoyanov, D. Mateus, M. A. Zuluaga, S. K. Zhou, D. Racoceanu, and L. Joskowicz, Eds. Cham: Springer International Publishing, 2020, pp. 299–308.
- [21] Q. Ma, L. Li, E. C. Robinson, B. Kainz, D. Rueckert, and A. Alansary, "CortexODE: Learning Cortical Surface Reconstruction by Neural ODEs," *IEEE Transactions on Medical Imaging*, vol. 42, no. 2, pp. 430–443, Feb. 2023.

- [22] F. Laumer, M. Amrani, L. Manduchi, A. Beuret, L. Rubi, A. Dubatovka, C. M. Matter, and J. M. Buhmann, “Weakly supervised inference of personalized heart meshes based on echocardiography videos,” *Medical Image Analysis*, vol. 83, p. 102653, 2023.
- [23] J. Xu, D. Moyer, B. Gagoski, J. E. Iglesias, P. E. Grant, P. Golland, and E. Adalsteinsson, “NeSVoR: Implicit Neural Representation for Slice-to-Volume Reconstruction in MRI,” *IEEE Transactions on Medical Imaging*, vol. 42, no. 6, pp. 1707–1719, Jun. 2023.
- [24] B. Song, L. Shen, and L. Xing, “PINER: Prior-Informed Implicit Neural Representation Learning for Test-Time Adaptation in Sparse-View CT Reconstruction,” in *Proceedings of the IEEE/CVF Winter Conference on Applications of Computer Vision*, 2023, pp. 1928–1938.
- [25] H. Li, H. Chen, W. Jing, Y. Li, and R. Zheng, “3D Ultrasound Spine Imaging with Application of Neural Radiance Field Method,” in *2021 IEEE International Ultrasonics Symposium (IUS)*, Sep. 2021, pp. 1–4.
- [26] P.-H. Yeung, L. Hesse, M. Aliasi, M. Haak, W. Xie, A. I. Namburete *et al.*, “Implicitvol: Sensorless 3d ultrasound reconstruction with deep implicit representation,” *arXiv preprint arXiv:2109.12108*, 2021.
- [27] J. J. Park, P. Florence, J. Straub, R. Newcombe, and S. Lovegrove, “DeepSDF: Learning Continuous Signed Distance Functions for Shape Representation,” in *Proceedings of the IEEE/CVF Conference on Computer Vision and Pattern Recognition*, 2019, pp. 165–174.
- [28] M. Baorui, H. Zhizhong, L. Yu-Shen, and Z. Matthias, “Neural-pull: Learning signed distance functions from point clouds by learning to pull space onto surfaces,” in *International Conference on Machine Learning (ICML)*, 2021.
- [29] R. S. Cruz, L. Lebrat, P. Bourgeat, C. Fookes, J. Frupp, and O. Salvado, “DeepCSR: A 3D Deep Learning Approach for Cortical Surface Reconstruction,” in *2021 IEEE Winter Conference on Applications of Computer Vision (WACV)*, Jan. 2021, pp. 806–815.
- [30] J. Sander, B. D. De Vos, S. Bruns, N. Planken, M. A. Viergever, T. Leiner, and I. Išgum, “Reconstruction and completion of high-resolution 3D cardiac shapes using anisotropic CMRI segmentations and continuous implicit neural representations,” *Computers in Biology and Medicine*, vol. 164, p. 107266, Sep. 2023.
- [31] D. Wiesner, J. Suk, S. Dummer, T. Nečasová, V. Ulman, D. Svoboda, and J. M. Wolterink, “Generative modeling of living cells with SO(3)-equivariant implicit neural representations,” *Medical Image Analysis*, vol. 91, p. 102991, Jan. 2024.
- [32] W. E. Lorensen and H. E. Cline, “Marching cubes: A high resolution 3D surface construction algorithm,” *ACM SIGGRAPH Computer Graphics*, vol. 21, no. 4, pp. 163–169, Aug. 1987.
- [33] F. Bernard, L. Salamanca, J. Thunberg, A. Tack, D. Jentsch, H. Lamecker, S. Zachow, F. Hertel, J. Goncalves, and P. Gemmar, “Shape-aware surface reconstruction from sparse 3D point-clouds,” *Medical Image Analysis*, vol. 38, pp. 77–89, May 2017.
- [34] H.-B. Chen, R. Zheng, L.-Y. Qian, F.-Y. Liu, S. Song, and H.-Y. Zeng, “Improvement of 3-D Ultrasound Spine Imaging Technique Using Fast Reconstruction Algorithm,” *IEEE Transactions on Ultrasonics, Ferroelectrics, and Frequency Control*, vol. 68, no. 10, pp. 3104–3113, Oct. 2021.
- [35] F. Zhao, W. Wang, S. Liao, and L. Shao, “Learning Anchored Unsigned Distance Functions With Gradient Direction Alignment for Single-View Garment Reconstruction,” in *Proceedings of the IEEE/CVF International Conference on Computer Vision*, 2021, pp. 12 674–12 683.
- [36] G. Chou, I. Chugunov, and F. Heide, “Gensdf: Two-stage learning of generalizable signed distance functions,” in *Proc. of Neural Information Processing Systems (NeurIPS)*, 2022.
- [37] X. Mao, Q. Li, H. Xie, R. Y. Lau, Z. Wang, and S. Paul Smolley, “Least squares generative adversarial networks,” in *Proceedings of the IEEE International Conference on Computer Vision (ICCV)*, Oct 2017.
- [38] H. Chen, R. Zheng, E. Lou, and L. H. Le, “Compact and Wireless Freehand 3D Ultrasound Real-time Spine Imaging System: A pilot study,” in *2020 42nd Annual International Conference of the IEEE Engineering in Medicine Biology Society (EMBC)*, Jul. 2020, pp. 2105–2108.
- [39] J. Li, Y. Huang, S. Song, H. Chen, J. Shi, D. Xu, H. Zhang, M. Chen, and R. Zheng, “Automatic Diagnosis of Carotid Atherosclerosis Using a Portable Freehand 3D Ultrasound Imaging System,” Jan. 2023.
- [40] J. Alavi, H. Chen, K.-C. T. Nguyen, T.-G. La, L. Kumaralingam, K. Punithakumar, M. Alexiou, E. H. Lou, M. Noga, P. W. Major, and L. H. Le, “Three-dimensional Intraoral Imaging using a Portable 3D Freehand Ultrasound System: A Phantom Study,” in *2023 IEEE International Ultrasonics Symposium (IUS)*, Sep. 2023, pp. 1–4.
- [41] P. Popescu-Pampu, *What Is the Genus?*, ser. Lecture Notes in Mathematics. Cham: Springer International Publishing, 2016, vol. 2162.